Research Square

Preprints are preliminary reports that have not undergone peer review.
They should not be considered conclusive, used to inform clinical practice,
or referenced by the media as validated information.

Preserved hydrothermal metal zoning in a deformed Besshi-type VMS system: Mineralogical and predictive evidence from the Hawiah deposit, Arabian Shield

Mario Kasha
King Fahd University of Petroleum and Minerals (KFUPM)
Basem Zoheir
basem.zoheir@gmail.com

King Fahd University of Petroleum and Minerals (KFUPM)
Astrid Holzheid
University of Kiel
Husam Baalousha
King Fahd University of Petroleum & Minerals (KFUPM)
Rhys Coles
Gold and Minerals Company Limited (GMCO)

Article

Keywords: Volcanogenic massive sulfides (VMS), Besshi type, Arabian Shield, metal mobilization, mineral chemistry, Random Forest

Posted Date: November 12th, 2026

DOI: https://doi.org/10.21203/rs.3.rs-11413853/v1

License: This work is licensed under a Creative Commons Attribution 4.0 International License.
Read Full License

Additional Declarations: No competing interests reported.

Preserved hydrothermal metal zoning in a deformed Besshi-type VMS system: Mineralogical and predictive evidence from the Hawiah deposit, Arabian Shield

Mario Kasha[1], Basem Zoheir[1,*], Astrid Holzheid[2], Husam Baalousha[3], Rhys Coles[4]

[1]*Department of Geosciences, College of Petroleum Engineering and Geosciences (CPG), King Fahd University of Petroleum and Minerals (KFUPM), 31261 Dhahran, Saudi Arabia*

[2]*Institute of Geosciences, University of Kiel, Ludewig-Meyn Str. 10, 24118 Kiel, Germany*

[3]*Interdisciplinary Research Center for Membranes and Water Security (IRC-MWS), King Fahd University of Petroleum & Minerals (KFUPM), Dhahran 31261, Saudi Arabia;*

[4]*Gold and Minerals Company Limited (GMCO), Bisha, Asir Region, Saudi Arabia*

*Corresponding author: basem.zoheir@gmail.com

Abstract

Ancient volcanogenic massive sulfide (VMS) deposits commonly undergo deformation, metamorphism and fluid-assisted recrystallization that obscure primary hydrothermal architecture and complicate exploration. We separate preserved metal zonation from deformation-related redistribution in fresh massive sulfide at the Hawiah Besshi-type VMS deposit, Arabian Shield, by integrating ore microscopy, electron-microprobe analysis

(EPMA), whole-rock geochemistry, block-model grades, and Random Forest regression. Relict framboidal pyrite (Py1) records an early texture, whereas recrystallized pyrite (Py2) and fracture-controlled Cu-Zn±Pb sulfides document post-ore modification. Interstitial and fracture-hosted chalcopyrite indicates local Cu redistribution, yet a deposit-scale gradient persists: Cu and Co decrease northward, whereas Zn, Cd, Pb and As increase. Sphalerite Fe contents (9.8-14.3 mol% FeS) give apparent Fe-Zn temperatures of ~311-355 °C, reflecting re-equilibration of recrystallized ore, not depositional conditions. Random Forest models trained on southern-zone data reproduce Zn in the northern and central zones (R^2 = 0.902 and 0.697), reflecting persistent Zn-Cd covariance, although high values are underpredicted. EPMA shows near-detection-limit Au in pyrite and pyrrhotite, and the company's SEM studies report native gold, electrum, and sylvanite (<5-~20 μm), some within or associated with pyrite. Deformation can thus modify Cu distribution without erasing hydrothermal zoning in deformed VMS deposits, a framework seems applicable to deformed VMS systems globally.

Keywords: *Volcanogenic massive sulfides (VMS); Besshi type; Arabian Shield; metal mobilization; mineral chemistry; Random Forest*

1. Introduction

Volcanogenic massive sulfide (VMS) deposits are the lithified products of submarine hydrothermal systems developed in volcanic and volcano-sedimentary successions. Seawater enters permeable stratigraphic intervals and fault-fracture networks, circulates

through hotter portions of the volcanic crust, and undergoes progressive chemical modification by water-rock interaction. Studies of modern seafloor systems and altered oceanic crust show that this circulation can mobilize substantial Cu, Zn, Pb, Au, S, and associated trace elements from the reaction zone [1]-[2]. Ascent, cooling and phase separation of evolved seawater and further mixing of evolved seawater with fresh water promote sulfide saturation and precipitation at or beneath the seafloor, producing a feeder-stockwork system overlain by stratiform to lensoidal massive sulfide accumulations [3]-[4].

The mineral assemblage, metal endowment, and internal zonation of VMS deposits are controlled by the composition and permeability of the host succession, tectonomagmatic setting, fluid-rock reaction pathways, and the physical and chemical conditions of discharge [5]. Variations in substrate composition and subsurface flow paths can, for example, strongly influence the composition of hydrothermal precipitates and the relative enrichment of Cu, Zn, Pb, and trace metals [6]. Accordingly, VMS ores commonly comprise pyrite, pyrrhotite, chalcopyrite, sphalerite, and galena, with variable contents of Cu, Zn, Pb, Ag, Au, and locally critical metals such as Co, Cd, Ge, In, Se, and Te [2]-[4].

Within the VMS spectrum, the Besshi-type endmember is generally termed mafic-siliciclastic, siliciclastic-mafic, or pelitic-mafic [7]-[8]-[9]. It is characteristically associated with mafic volcanic or intrusive rocks interbedded with turbiditic siliciclastic, pelitic, or semipelitic strata, and commonly contains laterally persistent, strata-bound sulfide sheets dominated by pyrite and pyrrhotite with subordinate chalcopyrite, sphalerite, and minor galena [9]-[10]. Such systems commonly develop in extensional submarine environments, including back-arc basins, rifted arcs, and sedimented oceanic basins, where permeable volcanic-sedimentary successions and synvolcanic structures focus hydrothermal

circulation [3]-[11]. Nevertheless, assignment to the Besshi class should rest on the complete lithostratigraphic association, ore morphology, mineral assemblage, and tectonic setting, rather than on any single host-rock characteristic.

The geometry and composition of ancient VMS deposits commonly differ substantially from their original seafloor configuration. Post-depositional deformation may transpose primary contacts, fold or boudinage massive sulfide lenses, and localize strain within mechanically weak sulfide-rich layers; these processes can redistribute base metals along grain boundaries, fractures, and shear fabrics [12]. The degree of modification depends on sulfide rheology, metamorphic temperature, differential stress, strain localization, and fluid availability, as illustrated by metamorphosed VMS deposits in the Urals and Iberian Pyrite Belt [12]-[13]. Fluid-assisted replacement and late hydrothermal overprinting can further modify mineral textures and metal budgets, producing secondary sulfides along fractures and grain boundaries [14]. Consequently, primary hydrothermal zonation must be assessed through the integrated interpretation of ore textures, paragenesis, in-situ mineral chemistry, and bulk-rock geochemistry rather than from grade patterns alone [9]-[15].

The Arabian-Nubian Shield (ANS) is composed of a series of juvenile Neoproterozoic arc, back-arc, and ophiolitic terranes that have assembled during closure of the Mozambique Ocean and the final amalgamation of Gondwana (e.g., [16]-[17]-[18]). This evolution produced a diverse metallogenic record that includes VMS mineralization in submarine volcano-sedimentary successions and orogenic-gold systems associated principally with younger transpressional to brittle-ductile shear zones [19]-[20]. Although both deposit types may occur within the same broad structural corridors, their spatial association does not demonstrate a common hydrothermal origin. In the ANS, prolonged deformation,

metamorphism, and locally intrusive activity can overprint earlier VMS ores and remobilize metals, as documented for the Um Samiuki VMS deposit in Egypt [21].

The Hawiah deposit occurs in the Wadi Bidah Mineral District (WBMD) of the Asir Terrane, southwestern Saudi Arabia. The WBMD forms a north-trending belt approximately 70 km long and 20 km wide, in which volcanic, volcaniclastic, sedimentary, and intrusive rocks have been variably folded and affected by brittle-ductile deformation [22]. District-scale massive sulfide occurrences are stratabound and concentrated within the Group 2 felsic-volcaniclastic succession; their present distribution and geometry reflect post-mineralization folding, faulting, and shearing [22]-[23]. The district also contains separate gold-bearing quartz-vein and stringer occurrences, which should not automatically be equated with the VMS mineralizing event [20]-[24]. Hawiah is a steeply dipping, tabular Cu-Zn-Au-Ag sulfide lens hosted by a variably sheared metavolcanic and metasedimentary succession [25]-[26]. Its Besshi-type affinity is therefore evaluated here within its full, structurally modified volcanic-sedimentary context.

GMCO (2025) reports an estimated Hawiah mineral resource of approximately 36.2 Mt at 0.82 wt% Cu, 0.86 wt% Zn, 0.64 g/t Au, and 10.0 g/t Ag. In this study, the Camp Zone is defined as the southern, Cu-rich principal ore domain, whereas the Crossroads Zone denotes the northern domain in which Zn, Pb, Cd, As, and locally Au become more prominent. The Central Zone lies between Camp and Crossroads; we suggest that this zone is intersected by a diorite intrusion. This deposit-scale metal pattern may preserve part of the primary hydrothermal architecture, but it may also reflect variable metamorphic sulfide remobilization, intrusive-fluid overprint, and supergene modification [13]-[14].

Testing these alternatives at deposit scale depends on whole-rock multi-element datasets comprising thousands of samples and many correlated elements, whose covariance is only partly resolved by bivariate diagrams and linear statistics. Random Forest, an ensemble of decision trees grown on bootstrap resamples that ranks predictors by importance [27], outperformed neural networks and support vector machines in mineral prospectivity mapping [28]. Machine learning has since been applied to lithogeochemical and core-logging data from VMS districts [29]-[30], to basalt geochemistry as a guide to VMS fertility [31], and to pyrite generations in overprinted ores (e.g., [32]), although predictive performance may deteriorate against independent data [33]. No such model has been applied to whole-rock geochemistry from a deformed Besshi-type deposit. Transferring a model calibrated in one ore zone to the others tests whether multi-element covariance persists across a deformed orebody.

The present study integrates ore textures, in-situ mineral chemistry, bulk-rock multi-element geochemistry, block-model grade distributions, and predictive modelling to distinguish components of the Camp-central-Crossroads metal zonation that reflect primary VMS processes from those generated or modified during later geological overprinting. The resulting process-based framework provides exploration-relevant vectors for recognizing preserved hydrothermal gradients, prioritizing prospective extensions of Cu-rich and Zn–Pb–Au-enriched domains, and identifying structurally or fluid-remobilized high-grade shoots. More broadly, it offers a transferable approach for drill targeting and resource evaluation in Hawiah and other deformed VMS systems of the ANS.

2. Geological setting

The Hawiah area is situated within the WBMD of the Asir Terrane in the southwestern Arabian Shield (Fig. 1). The WBMD forms a north-trending corridor approximately 70 km long and 20 km wide within the broader Bidah belt, an early Cryogenian juvenile arc assemblage that extends for approximately 300 km along strike and reaches about 75 km in width [22]-[24]. The Bidah belt comprises volcanic, volcaniclastic, and sedimentary successions intruded by mafic to intermediate calc-alkaline rocks of the Buwwah suite; available intrusion ages constrain the principal arc-related magmatic activity to ca. 855–815 Ma [24]. Within the WBMD, three lithostratigraphic groups young westward: Group 1 mafic volcanic rocks, Group 2 felsic volcaniclastics, and Group 3 epiclastic rocks intercalated with felsic volcaniclastics [22]-[34]. These successions were subsequently affected by tight to isoclinal folding, penetrative S_0–S_1 schistosity, and north–south sinistral shearing along the Wadi Bidah shear zone, with later synthetic and antithetic faulting further disrupting primary stratigraphic and orebody geometries [22]-[24].

In the Hawiah area, the orebody is hosted principally by epidote-chlorite schist, which forms the dominant lithology in the central part of the mapped area (Fig. 1). Chlorite schist occupies a broad belt to the northeast, whereas intermediate volcaniclastic rocks crop out along the eastern margin. Metabasalt and metagabbro are most extensively exposed in the southeast. To the west and southwest, metasiltstone is interbedded with epidote-chlorite schist, while hornblende schist and hornblende-biotite schist define northeast-trending belts. Extensive Quaternary wadi alluvium obscures bedrock in the principal drainage corridors and should be considered when extrapolating surface relationships beneath cover.

The pervasive epidote-chlorite assemblage indicates that most of the Hawiah host succession experienced greenschist-facies metamorphism, consistent with regional observations from the WBMD [22]-[24]. Hornblende-bearing and hornblende-biotite schists, however, indicate locally higher-temperature conditions compatible with upper-greenschist- to lower-amphibolite-facies metamorphism. This metamorphic variability is important because recrystallization, strain partitioning, and fluid-assisted replacement may have modified sulfide textures and metal distributions differently across the deposit.

The Hawiah orebody occupies the eastern limb of a major anticline and is spatially associated with a shear corridor. It forms a steeply dipping, tabular sulfide lens that extends for approximately 4.5 km along strike and is generally 1-15 m thick. GMCO (2025) subdivides the lens into the southern (Camp Zone), the intervening Central Zone, and the northern (Crossroads Zone); a cross-cutting diorite intrusion attenuates and locally interrupts the Central Zone (Fig. 2). The Camp Zone represents the principal Cu-rich domain, whereas the Crossroads Zone is characterized by relatively greater Zn, Pb, Cd, As, and locally Au enrichment. The steep foliation, shear-zone association, and attenuated geometry collectively indicate substantial ductile modification of the primary sulfide body, consistent with the post-mineralization folding and shearing documented elsewhere in the WBMD by [22]-[23].

Down-dip, the Hawiah orebody is divided into oxide, transitional, and fresh-sulfide zones (Fig. 2). The oxide zone is characterized by ferruginous gossan, chert, saccharoidal silica, and bleached wall rock; relative to fresh ore, it is locally enriched in Au and depleted in Ag. The transitional zone occurs principally between approximately 30 and 70 m below the surface and records progressive replacement of friable, porous, oxidized material by

178 coherent massive sulfide with depth. Fresh ore is fine-grained and dominated by pyrite, with
179 chalcopyrite and sphalerite as the principal Cu- and Zn-bearing phases. Magnetic and self-
180 potential data independently delineate the shallow sulfide-rich corridor and its oxidation-
181 related contrasts, supporting the down-dip zonation defined by drilling and geological
182 modelling [26]. Recognition of these supergene and structural domains is essential for drill
183 targeting, grade interpretation, and discrimination between primary metal zonation and
184 near-surface modification.

185

186 **3. Materials and methods**

187 *3.1. Sample selection and ore microscopy*

188 The three-dimensional Hawiah deposit model was used to guide sampling of fresh
189 massive sulfide intersected by diamond-drill core. To isolate deformation-, recrystallization-
190 , and fluid-assisted metal redistribution within the sulfide orebody, sampling in the present
191 study was restricted to fresh massive sulfide. Oxidized and transitional material was
192 excluded; therefore, supergene alteration and the mineralogical deportment of Au in the
193 gossan profile are outside the scope of this investigation. Seventy-three representative
194 samples were selected from the Camp, central, and Crossroads zones to capture variation in
195 depth, Cu grade, ore texture, and sulfide assemblage. Polished sections were examined by
196 reflected-light microscopy and back-scattered electron (BSE) imaging to establish mineral
197 associations, textural relationships, deformation fabrics, and sites suitable for in-situ
198 analysis.

3.2. Electron-microprobe analysis of ore minerals

Major, minor, and selected trace-element concentrations in pyrite, chalcopyrite, pyrrhotite, and sphalerite were determined using a JEOL JXA-iSP100 electron microprobe at the GEOMAR Helmholtz Centre for Ocean Research, Kiel, Germany. Polished sections were carbon coated before analysis. Analytical spots were selected from reflected light and BSE images to avoid fractures, mineral inclusions, alteration products, and phase boundaries.

Analyses were acquired by wavelength-dispersive spectrometry at an accelerating voltage of 15 kV, a beam current of 20 ηA, and a nominal beam diameter of 1 μm; peak-counting times were 20 s. Target elements comprised S, Fe, Cu, Zn, Pb, As, Se, Ag, Au, Cd, Sb, Sn, Ni, and Mn. Appropriate reference materials were repeatedly analyzed as unknowns during each analytical session to assess instrumental drift, precision, and accuracy. Analyses with low totals, image-detected contamination by adjacent phases, or concentrations below element-specific detection limits were excluded from quantitative interpretation. The resulting dataset was evaluated together with petrographic and BSE-textural evidence to distinguish primary compositional variation from compositions affected by recrystallization, replacement, or late fluid ingress.

3.3. Random Forest Model

Random Forest regression was used to predict Au, Ag, Cu, Zn, As, and Pb concentrations from 20 major- and trace-element predictor variables: Al, Ba, Be, Bi, Ca, Cd, Co, Cr, Fe, K, Mg, Mn, Mo, Na, Ni, P, S, Sr, Ti, and V in three drill-core datasets. The Camp-Zone dataset (n = 1,444) served as the reference for model training, and the Central (n = 82) and Crossroads (n = 3,144) datasets were treated as prediction targets. Antimony and Sc were excluded

because too few determinations were available; sample-identifier and depth fields were excluded from the models and retained only for traceability. Missing predictor values, which affect Bi in up to 42% of intervals, were replaced by medians computed from the reference dataset, and the same medians were applied to the Central and Crossroads datasets to prevent information leakage [35]. Intervals lacking a value for a given response element were omitted from that element's model, leaving 1,150-1,155 intervals for training. Predictors were then standardized using a scaler fitted to the training partition only.

Random Forest combines many regression trees, each grown on a bootstrap resample of the training data with a random subset of K predictors considered at each node; the ensemble prediction is the mean of the individual tree outputs rather than the majority vote used in classification [27]-[36]-[37]. For each response element, a model of 300 trees with unrestricted depth, a minimum of five samples to split a node, and 42 fixed random seeds was trained on a random 80:20 partition of the reference dataset. Performance was assessed on the 20% hold-out partition and by five-fold cross-validation of the training partition using the coefficient of determination (R^2), root-mean-square error (RMSE), and mean absolute error (MAE), together with residual and predicted-versus-measured plots. Predictions for the Central and Crossroads zones were taken as the mean of the 300 trees, and the standard deviation and 10^{th}-90^{th} percentile range of the tree outputs were retained as measures of uncertainty [38]. Predictor contributions were quantified as the mean decrease in node impurity and, because this measure can be biased [39], compared with Pearson correlation coefficients. All computations were performed in Python using scikit-learn [40].

4. Results

4.1. Ore mineralogy and textural variations

The Hawiah massive sulfide ores comprise pyrite, pyrrhotite, chalcopyrite, and sphalerite, with accessory galena. This assemblage is compatible with the pyrite–pyrrhotite-rich mineralogy commonly reported from mafic-siliciclastic (Besshi-type) VMS systems [7]-[9]. However, the observed textures do not represent an unmodified seafloor assemblage. Reflected-light microscopy of all three zones and BSE imaging of representative Camp and Crossroads samples reveal superimposed brittle deformation, sulfide recrystallization, and local redistribution of base-metal sulfides.

Pyrite is volumetrically dominant throughout the Camp, central, and Crossroads zones. Two textural populations are distinguished. Py1 comprises coarse, porous, anhedral to subhedral grains and locally preserves relict framboidal and colloform-derived textures. In the Camp Zone, sphalerite encloses fine-grained framboidal pyrite cores (Fig. 3A), whereas Crossroads samples retain disrupted colloform remnants within fractured pyrite aggregates (Fig. 3B). These textures are interpreted as vestiges of the early sulfide framework. Py2 is finer grained and typically euhedral to subhedral; it occurs along fractures and grain boundaries in Py1 and locally forms equigranular mosaics between earlier sulfides (Fig. 3C).

BSE imaging demonstrates that recrystallization is more extensive than suggested by reflected-light microscopy alone. In Camp-Zone samples, pyrite commonly forms polygonal, granoblastic mosaics with approximately 120° triple junctions, indicating static to syn-deformational annealing of the sulfide framework. Chalcopyrite, and less commonly sphalerite, occupies interstitial sites between recrystallized pyrite grains (Fig. 4A, D). Coarse

pyrite porphyroblasts locally enclose rounded chalcopyrite and pyrrhotite inclusions, consistent with sulfide entrapment during pyrite growth or recrystallization. Comparable mineralogical reorganization, including recrystallization and preferential redistribution of more ductile base-metal sulfides, has been documented in metamorphosed VMS deposits elsewhere [12]-[13].

Pyrrhotite is widespread but subordinate to pyrite in all zones. It occurs as irregular interstitial patches between pyrite grains (Figs. 3D, 4A), as rounded inclusions within pyrite porphyroblasts, and as thin grain-boundary films or equant grains in the Crossroads Zone (Fig. 4C). Curved pyrrhotite–chalcopyrite contacts and pyrrhotite relics enclosed by chalcopyrite are common. The rounded morphology of inclusions contrasts with the matrix-conforming habit of interstitial pyrrhotite, suggesting that pyrrhotite retained relatively greater mobility than the recrystallized pyrite framework during post-ore modification.

Several Camp-Zone samples contain dense mats of acicular actinolite enclosed within the chalcopyrite-sphalerite matrix (Figs. 3E, 4B). Chalcopyrite fills the interstices between actinolite laths and locally truncates them. The weak preferred orientation of the actinolite is consistent with greenschist-facies recrystallization during ductile deformation. Its enclosure by chalcopyrite indicates that Cu-bearing sulfide remained mobile during, or after, at least part of the actinolite-forming event; the precise timing of this relationship is evaluated further using mineral-chemical data.

Chalcopyrite provides the clearest textural distinction among the three ore zones. In the Camp Zone, it is abundant and locally forms a continuous interstitial matrix that envelops pyrite porphyroclasts and connects the granoblastic pyrite mosaic (Fig. 4A). Chalcopyrite also forms stringers that cross-cut Py1 (Fig. 3F) and it occurs as fine blebs and veinlets within

sphalerite, described here as *chalcopyrite disease* (Fig. 3G). These relations demonstrate that Cu-bearing sulfide was redistributed through the recrystallized ore framework. In the Crossroads Zone, chalcopyrite is subordinate and occurs mainly as thin rims around pyrite or as interstitial grains between fractured pyrite porphyroclasts; local coarsening is restricted to pyrrhotite-bearing embayments (Fig. 4C). Chalcopyrite is least abundant in the Central Zone, where it is confined principally to fracture-controlled veinlets.

Sphalerite is volumetrically subordinate in all zones. In the Camp Zone, larger grains commonly display embayed or pointed margins against chalcopyrite and locally survive as isolated remnants within the chalcopyrite-rich matrix (Fig. 3G). In the Crossroads Zone, sphalerite occurs mainly as small interstitial grains associated with chalcopyrite and, less commonly, pyrrhotite (Fig. 4C). Although these relationships are consistent with partial replacement or recrystallization, the relative contributions of exsolution, replacement, and deformation-assisted remobilization require confirmation from mineral chemistry.

Galena is a trace phase but occurs in several textural settings. In Camp Zone samples, it forms bright irregular films and stringers along pyrite grain boundaries and triple junctions, as well as small interstitial grains in contact with sphalerite and chalcopyrite (Fig. 4D). In the Crossroads Zone, galena is associated principally with sphalerite and Py2 (Fig. 3H). Its preferential occurrence along recrystallized grain boundaries and within interstitial networks suggests localized Pb redistribution during late-stage recrystallization or fluid-assisted modification, rather than preservation of a wholly primary galena distribution.

No discrete gold particles were observed by reflected-light microscopy or BSE imaging in the representative fresh-sulfide samples examined in this study. The occurrence of Au detected by EPMA in pyrite is described below.

311 The three zones preserve the post-ore history to different degrees. The Camp Zone
312 contains the most texturally diverse assemblage, in which fractured Py1 is locally healed by
313 Py2 and subsequently incorporated into polygonal pyrite mosaics. This association records
314 an early brittle component followed by pervasive recrystallization and ductile sulfide
315 reorganization. The Crossroads Zone is dominated by fractured pyrite porphyroclasts
316 enclosed in a finer-grained Py2-rich matrix, with base-metal sulfides concentrated in the
317 interstitial network (Fig. 3I). The Central Zone is the most strongly modified: pyrite is
318 intensely fractured, chalcopyrite and sphalerite are restricted largely to late fracture
319 networks, and pyrrhotite is scarce. Its proximity to the diorite intrusion is consistent with a
320 local thermal and fluid-related overprint, but a direct genetic link requires support from
321 paragenesis and mineral-chemical data. Collectively, these textures establish the framework
322 for evaluating whether the present Cu–Zn–Pb distribution records primary hydrothermal
323 zonation, deformation-assisted remobilization, or superimposed intrusive-fluid
324 modification.

325

326 *4.2. Mineral chemistry*

327 4.2.1. Pyrite

328 Pyrite contains 47.05-48.45 wt% Fe (median 47.71 wt%) and 51.99-55.03 wt% S
329 (median 54.27 wt%). Recalculation of the analytical data yields a mean formula of $Fe_{1.01}S_{1.99}$.
330 Arsenic concentrations range from 0.04 to 0.17 wt%, with a median of 0.07 wt% and an
331 analytical detection limit of 0.02 wt%. Copper, Zn, and Ni are detected sporadically: Cu
332 reaches 0.21 wt%, Zn reaches 0.46 wt%, and Ni does not exceed 0.03 wt%. Gold was also
333 detected in pyrite, although concentrations are straddling the lower detection limit of the

electron microprobe (≤ 0.07% wt). These Au detections were recorded despite the absence of observed discrete gold particles in the examined sections.

4.2.2. Pyrrhotite

Pyrrhotite contains 60.68-61.44 wt% Fe and 39.47-40.15 wt% S. On an Fe + S basis, the analyses contain 46.67-47.19 at% Fe, with a median of 46.82 at% Fe. These values lie between the theoretical Fe proportions of Fe_7S_8 (46.67 at% Fe) and Fe_9S_{10} (47.37 at% Fe). Arsenic concentrations range from 0.05 to 0.11 wt%. Copper reaches 0.42 wt% in a Crossroads-Zone analysis, whereas Zn reaches 0.50 wt% in a Camp-Zone analysis. Both maximum values were recorded from spots located close to chalcopyrite and sphalerite, respectively. A few analyses show trace Au contents (up to 0.09 wt%).

4.2.3. Chalcopyrite

Chalcopyrite contains 33.37-34.71 wt% Cu, 30.44-32.16 wt% Fe, and 34.48-35.43 wt% S. Recalculation to four atoms gives a mean formula of $Cu_{1.00}Fe_{1.01}S_{1.99}$. Arsenic is present at 0.05-0.11 wt%, whereas Se reaches a maximum of 0.31 wt%. Median Se is 0.085 wt% in Camp-Zone chalcopyrite and 0.030 wt% in Crossroads-Zone chalcopyrite. Nickel is detected only sporadically and does not exceed 0.03 wt%.

4.2.4. Sphalerite

Sphalerite contains 58.94-61.64 wt% Zn, 5.71-8.42 wt% Fe, and 33.05-33.50 wt% S. These compositions correspond to 9.78-14.26 mol% FeS, with a median of 12.78 mol% FeS. The median calculated formula, normalized to two atoms, is $(Zn_{0.87}Fe_{0.13})S$. Cadmium ranges from 0.02 to 0.26 wt%, with a median of 0.13 wt%. Copper ranges from below the detection limit to 1.46 wt%; the highest concentrations occur in grains containing visible chalcopyrite

356 inclusions or chalcopyrite-rich margins. Median FeS contents are 12.6 mol% in Camp-Zone
357 sphalerite and 13.0 mol% in Crossroads-Zone sphalerite.

358 4.2.5. Sphalerite geothermometry

359 The empirical Fe/Zn calibration of [41] gives approximately 311-355 °C (mean 336 ±
360 11 °C) as formation temperature for the Hawiah sphalerite, with no meaningful difference
361 between the two zones. That calibration is based on sphalerite precipitated directly from
362 modern vent fluids, whereas the Hawiah sulfides have been deformed and recrystallized, so
363 these values are regarded as re-equilibration temperatures rather than primary depositional
364 temperatures. Both the sphalerite and the near-Fe_7S_8 pyrrhotite compositions record
365 equilibration below peak metamorphic conditions, although monoclinic pyrrhotite implies
366 continued re-equilibration to lower temperatures during cooling.

367

368 *4.3. Whole rock multi-element Geochemistry*

369 Copper concentrations differ among the three ore zones (Fig. 5A). Camp and Central
370 samples have median Cu concentrations of approximately 10,000-11,000 ppm, whereas the
371 Crossroads-Zone median is approximately 4,500 ppm. Camp samples display the broadest
372 Cu interquartile range. On the Cu-Ag plot, Camp samples define an array extending from
373 approximately 100 to 100,000 ppm Cu and from 1 to 30 ppm Ag (ESM Fig. S1A). Central
374 samples occupy a narrower field along a similar trend, whereas Crossroads samples occur
375 predominantly at lower Cu concentrations. Cu-Pb and Cu-Zn plots show weak relationships
376 across all three zones (ESM Figs. S1B, C).

Zinc, Pb, and Cd display distinct zone-level distributions. Median Zn concentrations are approximately 2,800 ppm in the Central Zone, 3,500 ppm in the Camp Zone, and 5,500 ppm in the Crossroads Zone. Median Pb concentrations are approximately 250 ppm in the Central Zone, 200 ppm in the Crossroads Zone, and 100 ppm in the Camp Zone. Median Cd is approximately 15 ppm in the Crossroads Zone and approximately 7 ppm in the Central Zone (Figs. 5A, B).

The Pb-Zn plot shows positive arrays in all three zones, particularly in Camp and Crossroads samples (Fig. 6A). The Cd-Zn plot defines the strongest linear relationship in the dataset, extending from approximately 0.5 to 300 ppm Cd and 100 to 100,000 ppm Zn (Fig. 6B). Positive Zn-Ag and Pb-Ag trends are most evident in Crossroads samples, where Pb ranges from approximately 10 to 3,000 ppm and Zn from approximately 100 to 100,000 ppm (ESM Figs. S1D, E).

Median Ag concentrations range from approximately 8 to 15 ppm across the deposit, with the highest median in the Central Zone. Median Au concentrations range from approximately 0.4 to 0.6 ppm and are higher in the Central and Crossroads zones than in the Camp Zone (Fig. 5A). Median As increases from approximately 130 ppm in the Camp Zone to approximately 200 ppm in the Central Zone and approximately 300 ppm in the Crossroads Zone.

The Au-As plot shows positive arrays in the Camp and Crossroads zones (Fig. 6C). Camp samples range from approximately 30 to 700 ppm As and 0.1 to 2 ppm Au, whereas Crossroads samples extend to approximately 1,000 ppm As. Central Zone samples are more dispersed. Au and Ag are positively correlated in all three zones over ranges of approximately 0.1-2 ppm Au and 1-30 ppm Ag, with the clearest trend in the Crossroads Zone (Fig. 6D). Au-

400 Cu, Au-Pb, and Au-Zn plots are predominantly scattered, although weak positive trends occur
401 in Crossroads samples (ESM Figs. S1F-H).

402 Median Co decreases from approximately 80 ppm in the Camp Zone to approximately 50
403 ppm in the Central Zone and <20 ppm in the Crossroads Zone. Manganese has median
404 concentrations of approximately 400 ppm in the Camp Zone, 100 ppm in the Central Zone,
405 and 250 ppm in the Crossroads Zone (Fig. 5C). Median Ni is highest in the Central Zone at
406 approximately 8 ppm, compared with approximately 3 ppm in the Camp Zone and 4 ppm in
407 the Crossroads Zone. Bi, Sb, and Sc have median concentrations of 3-12 ppm across the three
408 zones. Vanadium and Mo medians remain low, at approximately 3-9 ppm (Fig. 5B, C).

409 Iron has median concentrations of approximately 40 wt% in all three zones and narrow
410 interquartile ranges (Fig. 5D). Calcium has a median concentration of approximately 0.13
411 wt% in the Central Zone, compared with approximately 1 wt% in the Camp and Crossroads
412 zones. Magnesium medians are approximately 0.15 wt% in the Camp Zone, 0.03 wt% in the
413 Central Zone, and 0.05 wt% in the Crossroads Zone. Potassium and Ti concentrations are low
414 throughout the dataset and generally do not exceed 0.02 wt%.

415

416 *4.4. Grade distribution*

417 The block model depicts Hawiah as a steeply dipping, tabular massive sulfide body that
418 is traceable for approximately 4.5 km along a broadly north-south strike (Fig. 7). The
419 southern Camp Zone and northern Crossroads Zone form the two principal down-plunge
420 domains. The Camp Zone extends for approximately 1.5 km down-plunge to a depth of about
421 660 m below surface, whereas the Crossroads Zone extends for approximately 1.7 km to a

depth of about 830 m below surface. Both zones plunge at approximately 25° to the south and are generally 1-15 m thick, with thinning towards their margins. The intervening Central Zone is restricted to depths of approximately 50-340 m below surface.

Copper grades show a marked south-to-north variation along the orebody (Fig. 7A). The Camp Zone contains the most extensive Cu-rich blocks, with grades commonly between 1 and 3 wt% Cu and local values reaching 4.96 wt% Cu. Cu grades decrease northward through the Central Zone. In the Crossroads Zone, blocks with <1 wt% Cu predominate, although isolated higher-grade blocks occur locally.

Zinc grades display a contrasting spatial distribution (Fig. 7B). The Camp Zone contains predominantly low-Zn blocks, whereas Zn grades increase through the Central Zone and remain elevated in the upper and central parts of the Crossroads Zone. The most extensive Zn-rich blocks fall within the 2–3.5 wt% Zn range, and the maximum modelled Zn grade is 4.40 wt%.

Gold grades also vary along strike and down-dip (Fig. 7C). In the deeper Camp Zone, Au grades are generally <0.5 g/t. Higher Au grades occur northward, particularly near the upper parts of the orebody. The highest modelled Au values, ranging from 2 to 4 g/t, form a thin, laterally persistent band along the gossan zone, where modelled Cu and Zn grades are low to near zero.

4.5. Random Forest prediction of elemental concentrations

Separate Random Forest regression models were trained for Au, Ag, Cu, Zn, As, and Pb using the Camp Zone drill-core dataset (n = 1,444) and 20 major- and trace-element

444 predictor variables. Model performance, including RMSE and calibration statistics, is
445 summarized in Table 1 and Fig. 8A.

446 Among the six response variables, Zn returned the highest test-set coefficient of
447 determination (R^2 = 0.898), with a mean cross-validation score of 0.884 ± 0.026 (Figs. 8B, C).
448 Test-set R^2 values were 0.477 for Pb, 0.362 for As, 0.302 for Cu, 0.237 for Ag, and 0.168 for
449 Au; mean cross-validation R^2 was 0.360 ± 0.032 for Cu and 0.089 ± 0.168 for Ag (Fig. 8D).
450 Training-set R^2 values exceeded 0.82 for all six models, and the RMSE for Zn rose from 1,863
451 ppm in the training set to 3,569 ppm in the test set.

452 When applied to the Crossroads dataset (n = 3,144), the models returned R^2 values of
453 0.139 for Au, 0.278 for Ag, 0.514 for Cu, 0.902 for Zn, 0.601 for As, and 0.589 for Pb (Fig. 9A).
454 The corresponding Central Zone values (n = 82) were -0.613, -0.043, 0.364, 0.697, -0.043,
455 and 0.175 (Fig. 9B). The RMSE for Zn was 3,556 ppm in the Crossroads Zone and 5,050 ppm
456 in the Central Zone.

457 R^2 and RMSE were calculated on untransformed concentrations and are weighted toward
458 high-grade samples, so calibration was examined separately. In the Crossroads Zone,
459 regression of measured on predicted concentrations returns slopes of 1.32-1.54 and
460 negative intercepts for all six elements: high concentrations are underpredicted and low
461 concentrations overpredicted, with the regression line crossing the 1:1 line at ~1,000 ppm
462 for Zn and ~10,000 ppm for Cu. Predicted values accordingly span a narrower range than
463 measured values (Fig. 9A); few Cu predictions fall below ~2,000 ppm, and predicted As
464 rarely exceeds ~700 ppm. Central Zone slopes (0.60-1.54) rest on 82 samples and are poorly
465 constrained; Au and Ag predictions show no trend along the 1:1 line, Au is predominantly
466 overpredicted (Fig. 9B), and Pb residuals widen and become increasingly negative above

~800 ppm predicted Pb (Fig. 8F). A high R^2 therefore does not indicate unbiased prediction: Crossroads Zn combines $R^2 = 0.902$ with a slope of 1.35.

The Zn model depends almost entirely on Cd, which has a feature-importance value of 0.906, followed by Fe and Co at 0.017 each (Fig. 8E). Because Cd and the other predictors are determined in the same multi-element analysis as Zn, the model does not replace a Zn determination or estimate grade. It tests whether the Camp Zone Zn-Cd relationship holds in the other zones and flags samples whose measured Zn departs strongly from the predicted value.

5. Discussion

5.1. Metamorphic recrystallization and selective sulfide mobility

The Hawiah massive sulfide lens preserves both relict early ore textures and a pervasive post-ore structural overprint. Coarse, porous, and locally framboidal Py1 retains remnants of the original sulfide framework, whereas finer-grained Py2 occurs along fractures and grain boundaries in Py1 and locally forms polygonal, equigranular mosaics. The presence of Py2 in fractures indicates pyrite dissolution-reprecipitation or recrystallization after brittle disruption of Py1. Conversely, 120° triple junctions and straight pyrite grain boundaries in Camp Zone mosaics record annealing and textural equilibration under lower differential stress.

The pyrite textures are accompanied by marked spatial reorganization of the base-metal sulfides. Chalcopyrite occurs as interstitial matrix, grain-boundary films, fracture-related stringers, and local replacement-like domains, whereas pyrrhotite occurs both as rounded

inclusions in pyrite and as matrix-conforming interstitial grains. These contrasting habits indicate that the pyrite framework and the Cu-Fe sulfides did not respond uniformly to deformation. In particular, the interstitial and fracture-controlled chalcopyrite indicates redistribution of Cu-bearing sulfide after formation of much of the pyrite framework. The available petrographic evidence does not distinguish unequivocally between solid-state migration, dissolution-reprecipitation, and fluid-assisted transport; Hawiah may have experienced more than one of these processes.

Such multistage modification is well documented in deformed VMS systems. At Mobrun (Canada), greenschist-facies metamorphism produced brittle and ductile deformation, annealing, shear zones, vein systems, and local Au remobilization within an otherwise recognizable massive sulfide architecture [42]. At Pyhäsalmi (Finland), distinct mechanical and mixed-state remobilization stages were identified from cataclastic sulfides, grain-boundary pyrrhotite, attenuation, and fracture-filling sulfides [43]. The Hawiah association of fractured Py1, recrystallized Py2, interstitial chalcopyrite, and matrix pyrrhotite is consistent with a similarly composite deformation history. Comparable rheological partitioning between pyrite-rich frameworks and more deformable base-metal sulfides has also been documented in Iberian and Uralian VMS deposits [12]-[13].

The Camp Zone preserves the strongest evidence for this reorganization. Chalcopyrite forms extensive matrix domains around pyrite porphyroclasts and locally crosscuts Py1 as stringers, whereas sphalerite contains abundant chalcopyrite inclusions and embayed margins. These relations indicate that Cu was redistributed through the Camp Zone ore after pyrite fracturing and during, or after, recrystallization. The greater abundance of chalcopyrite in this zone may therefore reflect both original Cu enrichment and

superimposed concentration into structurally favorable sites. Accordingly, present Cu grade cannot be interpreted as a direct proxy for the primary hydrothermal Cu distribution without considering texture and structural position.

Actinolite-chalcopyrite relationships provide an additional temporal constraint. Actinolite occurs as acicular mats enclosed by chalcopyrite, and chalcopyrite locally fills interstices between, or truncates, actinolite laths. These relations demonstrate that at least part of the chalcopyrite post-dates actinolite crystallization or recrystallization. They do not, however, establish whether chalcopyrite moved at peak metamorphic conditions, during retrogression, or during a later fluid event. The apparent sphalerite temperatures of 311-355 °C should similarly be considered Fe-Zn re-equilibration estimates rather than primary VMS depositional temperatures. Pyrrhotite compositions lying between Fe_7S_8 and Fe_9S_{10} stoichiometries support Fe-deficient pyrrhotite but do not identify a polymorph or provide an independent temperature constraint. This distinction is important because metamorphosed Besshi-type deposits commonly record prolonged recrystallization and trace-element mobility during their tectonothermal evolution [9].

5.2. Deposit-scale metal zonation: preservation and modification

The Hawiah dataset identifies a first-order zonation that is expressed consistently in block-model grades, whole-rock geochemistry, ore mineralogy, and mineral chemistry. The Camp Zone contains the highest Cu and Co concentrations, the most extensive Cu-rich blocks, and the greatest abundance of chalcopyrite-rich matrix and fracture-related textures. The Crossroads Zone contains the highest Zn, Cd, and As concentrations and the most extensive Zn-rich blocks. Pb is elevated in both the Central and Crossroads zones, whereas Ag shows

its clearest positive relationships with Zn and Pb in the Crossroads dataset. These associations define a broad south-to-north transition from a Cu-Co-rich Camp domain to a Zn-Cd-As-rich Crossroads domain, with the Central Zone displaying a distinct intermediate character.

The Zn-Cd association is particularly robust because it is supported independently by bulk-rock and mineral-scale data. Cadmium and Zn define a near-linear relationship over several orders of magnitude in the whole-rock dataset, and sphalerite contains measurable Cd at 0.02-0.26 wt%. These observations identify sphalerite as the principal Cd-bearing phase at Hawiah. The Pb-Zn relationship and positive Zn-Ag and Pb-Ag arrays are consistent with a sphalerite-galena-bearing assemblage, although the mineral host of Ag remains unresolved. Bulk correlations alone cannot distinguish Ag hosted in galena, Ag-bearing sulfosalts, inclusions, or multiple mineral phases.

The most parsimonious interpretation is that Hawiah retains a broad primary hydrothermal metal gradient that has been modified locally by post-ore Cu redistribution. In a VMS system, Cu-rich and Zn-Pb-rich domains may reflect changes in temperature, fluid composition, permeability, and the position of precipitation relative to feeder pathways and seawater mixing zones. Such gradients can be lateral, vertical, or subsequently transposed by folding and faulting. At Hawiah, the coherent Zn-Cd association and Crossroads enrichment indicate that the sphalerite-rich component of the orebody has retained a deposit-scale distribution. By contrast, the concentration of chalcopyrite in Camp Zone interstices and fractures indicates that the present Cu distribution includes a secondary structural component.

This interpretation does not require the present orebody geometry to replicate the original seafloor configuration. [22]-[23] demonstrated that Wadi Bidah massive sulfide occurrences are stratabound within a felsic-volcaniclastic horizon and were subsequently folded, faulted, and sheared. Hawiah should therefore be assessed within a structurally modified stratigraphic lens rather than as an undeformed hydrothermal transect. The relative preservation of broad Zn- and Cd-rich domains despite local sulfide modification is consistent with studies showing that VMS deposits can retain large-scale chemical architecture after recrystallization and later fluid ingress [14]-[15]-[21].

The Central Zone provides an important test of this framework. It is thinner, shallower, transected by diorite, chemically depleted in Ca-Mg-bearing gangue relative to the Camp and Crossroads zones, and texturally more strongly modified. Its limited sample population and distinct alteration history preclude a simple interpolation between the two main ore domains. Detailed sampling across the diorite contacts, coupled with mineral chemistry and mass-balance analysis, is required to determine whether the Central Zone compositions reflect physical attenuation of the primary lens, intrusive-fluid modification, selective sulfide remobilization, or a combination of these processes.

5.3. Constraints on Au and Ag enrichment

Gold and Ag do not follow the same spatial patterns as the principal base metals. Gold is associated positively with As in the Camp and Crossroads datasets but has weaker relationships with Cu, Zn, and Pb. Silver is most closely associated with Zn and Pb in the Crossroads Zone. These patterns demonstrate co-enrichment at the bulk-rock scale but do not identify mineral hosts, paragenetic stages, or transport mechanisms.

The shallow Au-rich band is especially significant because it differs from the deeper Cu- and Zn-rich domains. It forms a thin, laterally persistent interval within the oxidized gossan zone, where modelled Cu and Zn grades are low to near zero. This spatial relationship is compatible with supergene modification, but it does not prove that Au enrichment is wholly supergene. A primary Au-bearing horizon, remobilization during deformation, late hypogene fluid activity, and weathering-related enrichment may all produce or modify Au-As associations at different scales.

This uncertainty is not unusual in VMS deposits. At Myra Falls, Au occurs as electrum in late veinlets and is associated with a discrete Au-Zn-Pb-As-Sb assemblage identified through petrography and fluid-inclusion work [44]. In contrast, the Hawiah dataset currently contains no identified Au mineral, no Au-host data at the grain scale, and no fluid-inclusion or isotope constraints on Au-bearing fluids. The Au-As relation should consequently be used as a targeting vector, not as evidence for Au incorporation in pyrite or any other single sulfide phase.

A phase-specific program is required to resolve the Au budget. Priority analyses should include BSE- and cathodoluminescence-guided mapping of fresh and oxidized ore, automated mineralogy or high-resolution SEM–EDS mapping, LA-ICP-MS traverses across As-bearing pyrite and associated sphalerite, galena, and chalcopyrite, and targeted search for electrum, tellurides, and Au-bearing sulfosalts. Comparative sampling of the oxide, transitional, and fresh-sulfide zones is essential because Au enrichment in one weathering domain cannot be extrapolated automatically to the primary orebody.

The regional setting further reinforces the need for caution. The Arabian–Nubian Shield contains both gold-bearing VMS and orogenic-gold systems, and gold-enriched oxide caps

603 may develop above auriferous VMS deposits [20]. Wadi Bidah also contains separate gold-
604 bearing quartz-vein and stringer occurrences within the wider structural corridor [24].
605 Their spatial proximity to Hawiah does not demonstrate a common hydrothermal event or
606 an orogenic-gold overprint. Such a conclusion requires direct evidence for Au-bearing veins
607 or replacement textures, identification of the Au host, and relative timing with respect to
608 deformation and oxidation.

609

610 *5.4. Value and limits of Random Forest transfer*

611 The Random Forest analysis provides a quantitative measure of multielement covariance
612 between the Camp reference dataset and the other Hawiah zones. It does not establish
613 mineral hosts or genetic processes. Zn is the most transferable response variable: its test-set
614 R^2 is 0.898, its cross-validation R^2 is 0.884 ± 0.026, and prediction remains strong in both the
615 Crossroads (R^2 = 0.902) and Central (R^2 = 0.697) zones. This stability is consistent with the
616 persistent Zn-Cd association documented in the whole-rock and sphalerite datasets.

617 Pb and As transfer moderately to the Crossroads Zone, whereas Au and Ag have lower
618 predictive performance. The Central Zone produces negative R^2 values for Au, Ag, and As and
619 only modest R^2 values for Cu and Pb. These outcomes show that a model calibrated using
620 Camp Zone geochemical relationships cannot be assumed to predict every element equally
621 across the deposit. The small Central Zone dataset (n = 82), its distinct structural setting, and
622 its diorite intersection are all potential contributors to reduced transferability, but the
623 present dataset cannot quantify the relative importance of these factors.

Feature-importance outputs require similarly cautious interpretation. Cd, Fe, and Co are the highest-ranked variables in the Zn model, but feature importance measures predictive association within the selected dataset rather than causality. This distinction is especially important when predictor variables are correlated or when several elements reside in the same mineral assemblage. The model does not independently demonstrate that Cd, Fe, or Co controlled Zn mineralization; it identifies variables that improve Zn prediction in the Camp Zone training data.

Machine-learning approaches can strengthen VMS exploration when model results are integrated with geological and mineralogical constraints. [31] used machine learning and feature-importance analysis to evaluate VMS fertility from basalt geochemistry, illustrating the value of transparent model interpretation and independent validation. However, their regional classification problem differs fundamentally from deposit-scale prediction of metal concentrations. At Hawiah, future models should use spatially independent validation, such as drillhole-, bench-, or block-based hold-out sets, rather than relying solely on random train–test partitions. Predictor selection should exclude the response element, document treatment of compositional data and censored values, and be evaluated separately in oxide, transitional, and fresh-sulfide material.

5.5. Genetic model and post-depositional evolution

Integration of ore textures, mineral chemistry, whole-rock geochemistry, and block-model grades permits a two-stage genetic model for the Hawiah deposit. Stage I records seafloor hydrothermal precipitation of a stratabound sulfide lens within a mafic volcano-sedimentary succession, now represented by epidote-chlorite schist. Relict framboidal and

colloform-derived Py1 constitutes the principal textural vestige of this stage. The first-order metal distribution indicates that the lens was zoned at the time of formation. The Camp Zone is characterized by Cu-Co enrichment and a chalcopyrite-pyrrhotite-pyrite assemblage, whereas the Crossroads Zone is enriched in Zn, Cd, and As and dominated by sphalerite-galena-pyrite (Fig. 10B). An analogous zonation at the ABM deposit, where a Cu-Co-rich chalcopyrite-pyrrhotite-pyrite core formed at ~270-350 °C and a Zn-Pb-Ag-rich pyrite-sphalerite margin formed below 270 °C [45], suggests that the Camp Zone occupied a more proximal, higher-temperature position relative to the principal upflow zone, and that the Crossroads Zone represents a cooler, more distal domain. Given the subsequent folding and shearing, the present south-to-north gradient may reflect either primary lateral zonation or vertical zonation transposed into the plane of the orebody. Stage II was initiated by E-W shortening, which folded the host succession into a north-trending anticline and positioned the ore lens on its eastern limb, within the epidote-chlorite schist horizon and the N-S sinistral Wadi Bidah shear zone (Fig. 10A) [22]. Actinolite enclosed in Camp Zone chalcopyrite is consistent with greenschist-facies conditions in the ore horizon, whereas sphalerite Fe-Zn compositions (311-355 °C) record re-equilibration below the metamorphic peak. Under these conditions, Py1 underwent brittle fracturing, Py2 nucleated along fractures and grain boundaries, and parts of the pyrite framework annealed to polygonal mosaics, while the mechanically weaker chalcopyrite, pyrrhotite, and galena were redistributed into interstitial and fracture-hosted sites. This redistribution is most pronounced in the Camp Zone, where the Cu-rich primary ore provided the largest chalcopyrite reservoir. Studies of other metamorphosed VMS deposits indicate that such remobilization involves both solid-state and fluid-assisted mechanisms but remains largely

confined to the orebody, over distances from <1 m to ~100 m [43]-[45]-[46] Stage II therefore modified the Cu distribution at the grain and ore-shoot scales without obliterating the deposit-scale Cu versus Zn-Cd gradient, which is most reliably preserved by the sphalerite-hosted Zn-Cd association.

The diorite intrusion transects the Central Zone and therefore post-dates sulfide deposition, although its timing relative to the principal folding and shearing remains unconstrained. It is accordingly treated as a local overprint on the Stage II assemblage rather than as a discrete paragenetic stage (Fig. 10B). The intrusion may have supplied heat and/or fluids that modified the adjacent ore. This remains a working hypothesis requiring contact-traverse mineral chemistry, immobile-element-normalized mass balance, alteration mineralogy, and geochronological testing. This interpretation is consistent with several characteristics of the Central Zone: the ore is thinner and restricted to shallower levels (~50-340 m below surface), pyrite is intensely fractured, chalcopyrite and sphalerite are largely confined to late fracture networks, Ca and Mg are depleted, median Ni and Ag concentrations are highest, and Random Forest models trained on Camp Zone data show their poorest transferability. Near the northern intrusive contact, fractured Py1 crosscut by chalcopyrite veinlets along shear planes (Fig. 3I) illustrates the fracture-controlled Cu attributed here to intrusion-related fluid flow. Comparable metal redistribution and local upgrading by later magmatic fluids have been documented at the Hongtoushan and Um Samiuki deposits [14]-[21]. A purely thermal overprint is, however, difficult to reconcile with the Central Zone assemblage. In contact-metamorphosed pyritic rocks, pyrite loses sulfur whereas pyrrhotite remains stable [47]; the scarcity of pyrrhotite in the Central Zone therefore implies that modification was predominantly fluid-controlled or occurred below the thermal threshold

693 of pyrite breakdown. Part of the mixed Cu–Zn signature of the Central Zone may also be
694 inherited from the primary system, given its intermediate position between the proximal and
695 distal domains. The limited Central Zone dataset (n = 82) and the absence of sampling
696 traverses across the intrusive contacts preclude discrimination among these alternatives,
697 and geochronology of the diorite, combined with mineral-chemical and mass-balance
698 analyses across its contacts, is required to test this component of the model. The present
699 erosion surface intersects the lens where the Central Zone is thinnest, and subsequent
700 weathering generated the oxide zone and the Au-rich gossan, which lie beyond the scope of
701 this fresh-sulfide study. The Hawiah deposit is thus best interpreted as a Besshi-type sulfide
702 lens with primary Cu to Zn-Cd zonation that was folded, sheared, and recrystallized under
703 greenschist-facies conditions and subsequently reworked locally adjacent to the diorite
704 intrusion.

705

706 *5.6. Implications for further exploration activities*

707 The results support a process-based exploration strategy that separates robust deposit-
708 scale vectors from local modification effects. In the Camp Zone, Cu and Co enrichment should
709 be assessed together with chalcopyrite abundance, pyrite recrystallization textures, fracture
710 density, and structural position. High Cu grades in this domain may indicate both original Cu
711 enrichment and local concentration of chalcopyrite during deformation. Cu grade alone
712 should therefore not be used to locate the original hydrothermal center.

713 In the Crossroads Zone, the Zn-Cd association provides the clearest vector for sphalerite-
714 rich mineralization. Pb-Zn-Ag relationships can be used to prioritize intervals for follow-up
715 mineralogical work, especially where galena and sphalerite are abundant. Because the

Crossroads Zone extends to greater depth than the Central Zone and retains coherent Zn-rich block-model domains, down-plunge continuity of Zn-Cd enrichment represents a priority exploration target.

The Central Zone requires a separate exploration model. Its restricted vertical extent, diorite intersection, altered Ca-Mg signature, and poor Random Forest transfer for several elements indicate that it should not be treated simply as an attenuated continuation of either Camp or Crossroads. Drilling should test geometry and alteration across intrusive contacts and should obtain sufficient fresh-sulfide samples to evaluate whether the apparent discontinuity reflects displacement, truncation, replacement, or limited sampling.

Gold exploration should proceed on two parallel tracks: shallow oxide-zone evaluation and fresh-sulfide Au-host characterization. The shallow Au-rich gossan band is an immediate near-surface target, whereas the Camp and Crossroads Au-As associations warrant systematic mineralogical analysis at depth. This approach avoids conflating near-surface enrichment with primary Au mineralization and provides the data needed to distinguish VMS-related Au from any later structural or weathering-related contribution.

6. Conclusions

1. Hawiah preserves deposit-scale VMS metal zonation within a strongly deformed and recrystallized sulfide lens with Besshi-type affinities. Post-ore modification was metal selective, with preferential chalcopyrite redistribution within the comparatively rigid pyrite framework, particularly in the Camp Zone. Its Cu enrichment is therefore best interpreted as an inherited primary signature modified by local structural and fluid-

assisted concentration. Cu tenor alone cannot uniquely locate the original hydrothermal center.

2. The Camp Cu-Co and Crossroads Zn-Cd-Pb-As signatures define complementary exploration domains. Persistent Zn–Cd coupling, supported by Cd-bearing sphalerite, provides a mineralogically constrained marker of the retained base-metal architecture. Zn-Pb-Ag relationships further associate Ag enrichment with the Crossroads sphalerite–galena assemblage. These associations remain useful exploration vectors when evaluated alongside sulfide textures and structural controls.

3. Gold has multiple mineralogical modes of occurrence. EPMA detected Au in pyrite and pyrrhotite in our representative samples, although no discrete gold particles were observed. Company-reported SEM and heavy-mineral separation studies document native gold, electrum, and sylvanite grains ranging from <5 to approximately 20 μm across, with native gold and sylvanite observed within or associated with pyrite. Their relative contributions to the Au inventory and paragenetic relationships remain unresolved. Shallow Au enrichment is spatially distinct from the deeper Cu-Zn domains and is consistent with weathering-related modification.

4. Random Forest transfer primarily demonstrates the persistence of Zn-Cd covariance across the studied zones. Calibration bias and weaker transferability for other metals constrain quantitative prediction, supporting the use of these models to identify geochemical departures and guide targeted verification. Exploration at Hawiah should integrate mineral-hosted metal associations, sulfide textures, structural setting, and oxidation profiles, with Au–As anomalies assessed within this geological framework.

761

762

Acknowledgements

The authors gratefully acknowledge GMCO for granting access to the Hawiah deposit and for providing drilling and assay data. Constructive discussions with GMCO geologists (i.e., Mahmoud Moustafa) were invaluable in developing a robust understanding of the deposit's geological and structural setting.

Author contributions

M.K. and B.Z. designed the study and carried out the fieldwork, sampling and analyses. M.K. and H.B. developed the models. M.K., B.Z. and H.B. interpreted the results and wrote the manuscript. B.Z., H.B. and A.H. supervised the study. B.Z., H.B. and R.C. performed the validation and visualization. All authors reviewed the manuscript.

Data availability

GMCO provided the drill-core assay and resource block-model datasets, as well as access to representative core samples. With the exception of the proprietary assay and block-model data, all raw data generated in this study are included in the Supplementary Tables.

Code availability

We used Python 3.12.5, numpy 1.26.4, pandas 2.2.2, scipy 1.14.1, scikit-learn 1.5.2, matplotlib 3.9.2, and openpyxl 3.1.5 to generate the Random forest models; the code and predictor list are available in https://github.com/mariokasha95-ai/hawiah-RF-codes.git.

Competing interests

R.C. is employed by GMCO, which provided some of the datasets used in this study. The remaining authors declare no competing interests.

Funding declaration

The authors would like to acknowledge the College of Petroleum Engineering & Geosciences (CPG), King Fahd University of Petroleum and Minerals (KFUPM), for supporting this work.

References

1. Humphris, S. E. & Cann, J. R. Constraints on the energy and chemical balances of the modern TAG and ancient Cyprus seafloor sulfide deposits. *J. Geophys. Res. Solid Earth* **105,** 28477–28488 (2000).
2. Patten, C. G. C., Pitcairn, I. K., Teagle, D. A. H. & Harris, M. Mobility of Au and related elements during the hydrothermal alteration of the oceanic crust: implications for the sources of metals in VMS deposits. *Miner. Depos.* **51,** 179–200 (2016).
3. Hannington, M. D., de Ronde, C. E. J. & Petersen, S. Sea-floor tectonics and submarine hydrothermal systems in *Economic Geology One Hundredth Anniversary Volume* (eds Hedenquist, J. W., Thompson, J. F. H., Goldfarb, R. J. & Richards, J. P.) 111–141 (Society of Economic Geologists, 2005).

4. Triantafyllidis, S. S. The mineralogy and geochemistry of volcanogenic massive sulfides and their contribution to human evolution: past, present and future. *Minerals* **16,** 486; https://doi.org/10.3390/min16050486 (2026).
5. Piercey, S. J. The setting, style, and role of magmatism in the formation of volcanogenic massive sulfide deposits. *Miner. Depos.* **46,** 449–471 (2011).
6. Sánchez-Mora, D., Jamieson, J., Cannat, M., Escartín, J. & Barreyre, T. Effects of substrate composition and subsurface fluid pathways on the geochemistry of seafloor hydrothermal deposits at the Lucky Strike vent field, Mid-Atlantic Ridge. *Geochem. Geophys. Geosyst.* **23,** e2021GC010073; https://doi.org/10.1029/2021GC010073 (2022).
7. Barrie, C. T. & Hannington, M. D. Classification of volcanic-associated massive sulfide deposits based on host-rock composition in *Volcanic-Associated Massive Sulfide Deposits: Processes and Examples in Modern and Ancient Settings* (eds Barrie, C. T. & Hannington, M. D.) Reviews in Economic Geology Vol. 8, 1–11 (Society of Economic Geologists, 1999).
8. Franklin, J. M., Gibson, H. L., Jonasson, I. R. & Galley, A. G. Volcanogenic massive sulfide deposits in *Economic Geology One Hundredth Anniversary Volume* (eds Hedenquist, J. W., Thompson, J. F. H., Goldfarb, R. J. & Richards, J. P.) 523–560 (Society of Economic Geologists, 2005).
9. Zacharias, J., Clark, P. & Kohler, M. Tracing the origin and P-T metamorphic history of the VMS Besshi-type Tisova deposit, Czech Republic: evidence for Co, As and Sb mobility. *Ore Geol. Rev.* **188,** 107050 (2026).

10. Slack, J. F., Shanks, W. C. III & Woodruff, L. G. Seeing through metamorphism: geochemical and isotopic studies of amphibolite facies mafic-siliciclastic (Besshi-type) massive sulfide deposits at the Elizabeth Copper Mine, Vermont, USA. *Econ. Geol.* **119,** 1487–1524 (2024).
11. Cox, D. P. & Singer, D. A. (eds) *Mineral Deposit Models*. U.S. Geological Survey Bulletin 1693 (U.S. Geological Survey, 1986).
12. Castroviejo, R., Quesada, C. & Soler, M. Post-depositional tectonic modification of VMS deposits in Iberia and its economic significance. *Miner. Depos.* **46,** 615–637 (2011).
13. Vikentyev, I. V., Belogub, E. V., Novoselov, K. A. & Moloshag, V. P. Metamorphism of volcanogenic massive sulphide deposits in the Urals. *Ore Geol. Rev.* **85,** 30–63 (2017).
14. Zhao, F., Gao, W., Huang, F. & Liu, B. Re-distribution and upgrade of metals induced by the superimposition of later magmatic fluids in the Archean Hongtoushan VMS deposit, NE China. *Ore Geol. Rev.* **167,** 105997 (2024).
15. Sun, C. et al. Tracing the formation and modification of the Keketale VMS-type Pb-Zn deposit, Altai Mountains: insights from ore deposit geology, geochronology, and magnetite geochemistry. *Ore Geol. Rev.* **144,** 104852 (2022).
16. Johnson, P. R., Abdelsalam, M. G. & Stern, R. J. The Bi'r Umq-Nakasib suture zone in the Arabian-Nubian Shield: a key to understanding crustal growth in the East African Orogen. *Gondwana Res.* **6,** 523–530 (2003).
17. Stoeser, D. B. & Frost, C. D. Nd, Pb, Sr, and O isotopic characterization of Saudi Arabian Shield terranes. *Chem. Geol.* **226,** 163–188 (2006).
18. Stern, R. J. & Johnson, P. R. Continental lithosphere of the Arabian Plate: a geologic, petrologic, and geophysical synthesis. *Earth-Sci. Rev.* **101,** 29–67 (2010).

19. Doebrich, J. L. et al. Geology and metallogeny of the Ar Rayn terrane, eastern Arabian Shield: evolution of a Neoproterozoic continental-margin arc during assembly of Gondwana within the East African orogen. *Precambrian Res.* **158,** 17–50 (2007).
20. Johnson, P. R. et al. Gold-bearing volcanogenic massive sulfides and orogenic-gold deposits in the Nubian Shield. *S. Afr. J. Geol.* **120,** 63–76 (2017).
21. Zoheir, B., Lohmeier, S., Tang, Y. & Martin, A. Geochemical and geochronological studies of the Um Samiuki deposit (Eastern Desert, Egypt): metal mobilization in a stratabound massive sulfide ore. *Ore Geol. Rev.* **166,** 105967 (2024).
22. Volesky, J. C., Stern, R. J. & Johnson, P. R. Geological control of massive sulfide mineralization in the Neoproterozoic Wadi Bidah shear zone, southwestern Saudi Arabia: inferences from orbital remote sensing and field studies. *Precambrian Res.* **123,** 235–247 (2003).
23. Volesky, J. C. et al. Metavolcanic host rocks, mineralization, and gossans of the Shaib al Tair and Rabathan volcanogenic massive sulphide deposits of the Wadi Bidah Mineral District, Saudi Arabia. *Int. Geol. Rev.* **59,** 1975–2002 (2017).
24. Johnson, P. R. & Kattan, F. H. *Geology of the Arabian Shield* (Saudi Geological Survey, 2012).
25. Kirmizakis, P. et al. Mapping sulphide mineralization in the Hawiah area using transient electromagnetic methods. *Minerals* **15,** 186; https://doi.org/10.3390/min15020186 (2025).
26. Salem, A., Chavanidis, K., Bryan, T., Eatwell, T. & Soupios, P. A magnetic signature of volcanogenic massive sulphide deposits: an example from the Hawiyah area, western Saudi Arabia. *Arab. J. Sci. Eng.* **51,** 20303–20319 (2026).

27. Breiman, L. Random forests. *Mach. Learn.* **45,** 5–32 (2001).

28. Rodriguez-Galiano, V., Sanchez-Castillo, M., Chica-Olmo, M. & Chica-Rivas, M. Machine learning predictive models for mineral prospectivity: an evaluation of neural networks, random forest, regression trees and support vector machines. *Ore Geol. Rev.* **71,** 804–818 (2015).

29. Caté, A., Schetselaar, E., Mercier-Langevin, P. & Ross, P.-S. Classification of lithostratigraphic and alteration units from drillhole lithogeochemical data using machine learning: a case study from the Lalor volcanogenic massive sulphide deposit, Snow Lake, Manitoba, Canada. *J. Geochem. Explor.* **188,** 216–228 (2018).

30. Schnitzler, N., Ross, P.-S. & Gloaguen, E. Using machine learning to estimate a key missing geochemical variable in mining exploration: application of the Random Forest algorithm to multi-sensor core logging data. *J. Geochem. Explor.* **205,** 106344 (2019).

31. Li, J. et al. High-accuracy mineralization evaluation of VMS deposits using machine learning and basalt geochemistry. *Ore Geol. Rev.* **184,** 106780 (2025).

32. Yu, P. et al. Machine learning of pyrite geochemistry reconstructs the multi-stage history of mineral deposits. *Geosci. Front.* **16,** 102011 (2025).

33. Behnia, P., Harris, J., Sherlock, R., Naghizadeh, M. & Vayavur, R. Mineral prospectivity mapping for orogenic gold mineralization in the Rainy River area, Wabigoon Subprovince. *Minerals* **13,** 1267; https://doi.org/10.3390/min13101267 (2023).

34. Béziat, P. & Donzeau, M. *The Mamilah–Wadi Bidah Mineral Belt: Geology and Mineral Exploration*. Open-File Report BRGM-OF-09-5 (Ministry of Petroleum and Mineral Resources, Deputy Ministry for Mineral Resources, 1989).

35. Kuhn, M. & Johnson, K. *Applied Predictive Modeling* (Springer, 2013).

36. Breiman, L., Friedman, J. H., Olshen, R. A. & Stone, C. J. *Classification and Regression Trees* (Wadsworth, 1984).
37. Breiman, L. Bagging predictors. *Mach. Learn.* **24,** 123–140 (1996).
38. Meinshausen, N. Quantile regression forests. *J. Mach. Learn. Res.* **7,** 983–999 (2006).
39. Strobl, C., Boulesteix, A.-L., Zeileis, A. & Hothorn, T. Bias in random forest variable importance measures: illustrations, sources and a solution. *BMC Bioinformatics* **8,** 25; https://doi.org/10.1186/1471-2105-8-25 (2007).
40. Pedregosa, F. et al. Scikit-learn: machine learning in Python. *J. Mach. Learn. Res.* **12,** 2825–2830 (2011).
41. Keith, M. et al. Effects of temperature, sulfur, and oxygen fugacity on the composition of sphalerite from submarine hydrothermal vents. *Geology* **42,** 699–702 (2014).
42. Larocque, A. C. L. & Hodgson, C. J. Effects of greenschist-facies metamorphism and related deformation on the Mobrun massive sulfide deposit, Québec, Canada. *Miner. Depos.* **30,** 439–448 (1995).
43. Islam, S. R., Heilimo, E., Kuva, J., Mäkilä, E. & Mäki, T. Decoding multiple ore mineral remobilization processes during polyphase deformational phases from the Precambrian Pyhäsalmi VMS deposit halo, Central Finland: new insights from mineralogy, mineral chemistry and micro-CT. *Int. J. Earth Sci.* **114,** 727–747 (2025).
44. Marshall, D. et al. Precious metal enrichment at the Myra Falls VMS deposit, British Columbia, Canada. *Geosciences* **8,** 422; https://doi.org/10.3390/geosciences8110422 (2018).

45. Denisová, N., Piercey, S. J. & Wälle, M. Mineralogy and mineral chemistry of the ABM replacement-style volcanogenic massive sulfide deposit, Finlayson Lake district, Yukon, Canada. *Miner. Depos.* **59,** 473–503 (2024).
46. Rincon, J. et al. Ore remobilization history of the metamorphosed Rävliden North volcanogenic massive sulfide deposit, Skellefte district, Sweden. *Econ. Geol.* **119,** 907–934 (2024).
47. Virtanen, V. J., Heinonen, J. S., Märki, L., Galvez, M. E. & Molnár, F. Sedimentary and metamorphic processes priming black shale for magmatic assimilation of sulfur: an example from the Virginia Formation, Minnesota, United States. *Miner. Depos.* **60,** 303–319 (2025).

Figure Legend

Fig. 1. Geological map of the Hawiah area (this study). Inset shows the location of Hawiah within the WBMD and the ANS, simplified after [24].

Fig. 2. East-looking longitudinal section through the Hawiah orebody model, showing the distribution of weathering domains and the Camp, central, and Crossroads zones. FR, fresh sulfide zone; TR, transitional zone; OXTR, oxide-transitional zone; Ox, oxide zone.

Fig. 3. Reflected-light photomicrographs of Hawiah massive sulfide ore, illustrating the principal sulfide assemblages and deformation-related textures. (**A**) Coarse Py1 adjacent to sphalerite enclosing fine-grained framboidal pyrite; minor pyrrhotite is interstitial, and chalcopyrite occupies grain boundaries, (**B**) Fractured and partly recrystallized pyrite retaining colloform-derived remnants, (**C**) Coarse Py1 bordered by pyrrhotite and intergrown with sphalerite and chalcopyrite; finer, euhedral Py2 occurs at left, (**D**) Anhedral pyrrhotite interstitial to pyrite, with sphalerite partly enclosed by chalcopyrite, (**E**) Acicular actinolite within a chalcopyrite-sphalerite matrix containing Py1 and Py2, (**F**) Coarse Py1 in massive chalcopyrite intergrown with pyrrhotite; sphalerite margins are embayed against chalcopyrite, (**G**) Sphalerite-rich domain containing coarse Py1 and fine-grained Py2, locally rimmed by chalcopyrite, (**H**) Interstitial galena associated with sphalerite, chalcopyrite, and Py2 adjacent to a larger Py1 grain, (**I**) Fractured Py1 porphyroclast cut by chalcopyrite veinlets along shear planes. Abbreviations: Act, actinolite; Ccp, chalcopyrite; Gn, galena; Po, pyrrhotite; Py1, coarse early pyrite; Py2, finer recrystallized pyrite; Sp, sphalerite.

Fig. 4. BSE images of sulfide assemblages from the Camp (**A, B, D**) and Crossroads (**C**) zones. (**A**) Polygonal, granoblastic pyrite mosaic enclosed by a continuous chalcopyrite matrix; anhedral pyrrhotite is interstitial, and sphalerite occurs at the base of the image. (**B**) Acicular actinolite adjacent to coarse pyrite; chalcopyrite fills interstices between laths and locally truncates them. (**C**) Pyrite enclosing a small interstitial cluster of chalcopyrite, sphalerite, and pyrrhotite. (**D**) Galena forming irregular grain-boundary films, stringers, and an interstitial grain in contact with sphalerite and chalcopyrite. Abbreviations: Act, actinolite; Ccp, chalcopyrite; Gn, galena; Po, pyrrhotite; Py, pyrite; Sp, sphalerite.

Fig. 5. Box-and-whisker plots showing whole-rock multi-element concentrations in the Camp, Central, and Crossroads zones of the Hawiah deposit. (**A**) Ag, As, Au, Cu, and Zn; (**B**) Bi, Cd, Pb, Sb, and Sc. Trace and minor elements are reported in ppm; major elements are reported in wt%. Boxes represent the interquartile range, central lines indicate medians, and points denote outliers. Concentration axes are logarithmic.

Fig. 5. Continued. Box-and-whisker plots showing whole-rock multi-element concentrations in the Camp, Central, and Crossroads zones of the Hawiah deposit. (**C**) Co, Mn, Mo, Ni, and V; and (**D**) Ca, Fe, K, Mg, and Ti. Trace and minor elements are reported in ppm; major elements are reported in wt%. Boxes represent the interquartile

range, central lines indicate medians, and points denote outliers. Concentration axes are logarithmic.

Fig. 6. Selected zone-resolved bivariate plots of whole-rock multi-element data from Hawiah.; (**A**) Pb-Zn, and (**B**) Cd-Zn. Camp-Zone samples are shown in orange, Central-Zone samples in blue, and Crossroads-Zone samples in grey. All concentrations are in ppm, and all axes are logarithmic.

Fig. 6 continued. Selected zone-resolved bivariate plots of whole-rock multi-element data from Hawiah. (**C**) As-Au, and (**D**) Ag-Au. Camp-Zone samples are shown in orange, Central-Zone samples in blue, and Crossroads-Zone samples in grey. All concentrations are in ppm, and all axes are logarithmic.

Fig. 7. East-looking block-model longitudinal section through the Hawiah orebody model, showing grade distributions in the Camp, Central, and Crossroads zones. (**A**) Cu grades (wt%). (**B**) Zn grades (wt%). (**C**) Au grades (g/t).

Table 1. Performance statistics for Random Forest regression models trained using the Camp Zone reference dataset.

Fig. 8. Random Forest model performance based on the Camp-Zone reference dataset. (**A**) Coefficients of determination for the reference test set and the Central and Crossroads prediction datasets. (**B**) Five-fold cross-validation results for Zn. (**C**) Predicted versus measured Zn concentrations for the training and test subsets. (**D**) Five-fold cross-validation results for Ag. (**E**) Feature-importance ranking for the Zn model. (**F**) Residual plot for Central-Zone predictions.

Fig. 9. Predicted versus measured concentrations of Au, Ag, Cu, Zn, As, and Pb for (**A**) the Crossroads Zone (n = 3,144) and (**B**) the Central Zone (n = 82). The dashed line indicates the 1:1 relationship.

Fig. 10. Geological cross-section and schematic genetic model for the formation and post-depositional evolution of the Hawiah deposit. (**A**) W-E cross-section along line A-A′ of the geological map in Fig. 1, looking north. The massive sulfide lens dips ~85° W and lies in epidote-chlorite schist on the eastern limb of the host anticline, within the N-S sinistral Wadi Bidah shear zone. Beds dip 80-88° W and faults dip 88° W. The orebody is projected onto the section along strike. (**B**) Conceptual working model showing the Zn-Pb-Cd-rich massive sulfide (Sp-Gn-Py) of the Crossroads zone, the Cu-rich massive sulfide (Ccp-Po-Py) of the Camp Zone, and the diorite intrusion that cuts the Central Zone, with its contact aureole, heat, and intrusion-related fluid pathways. Abbreviations: Py, pyrite; Ccp, chalcopyrite; Po, pyrrhotite; Sp, sphalerite; Gn, galena.

Figure 1

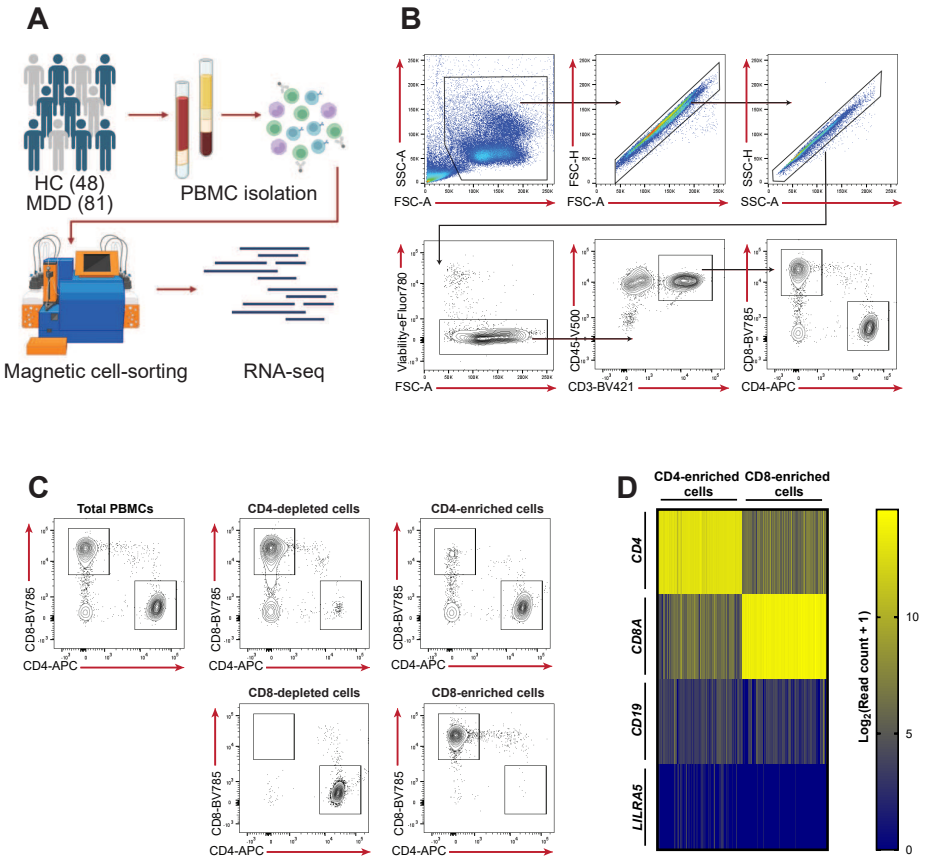
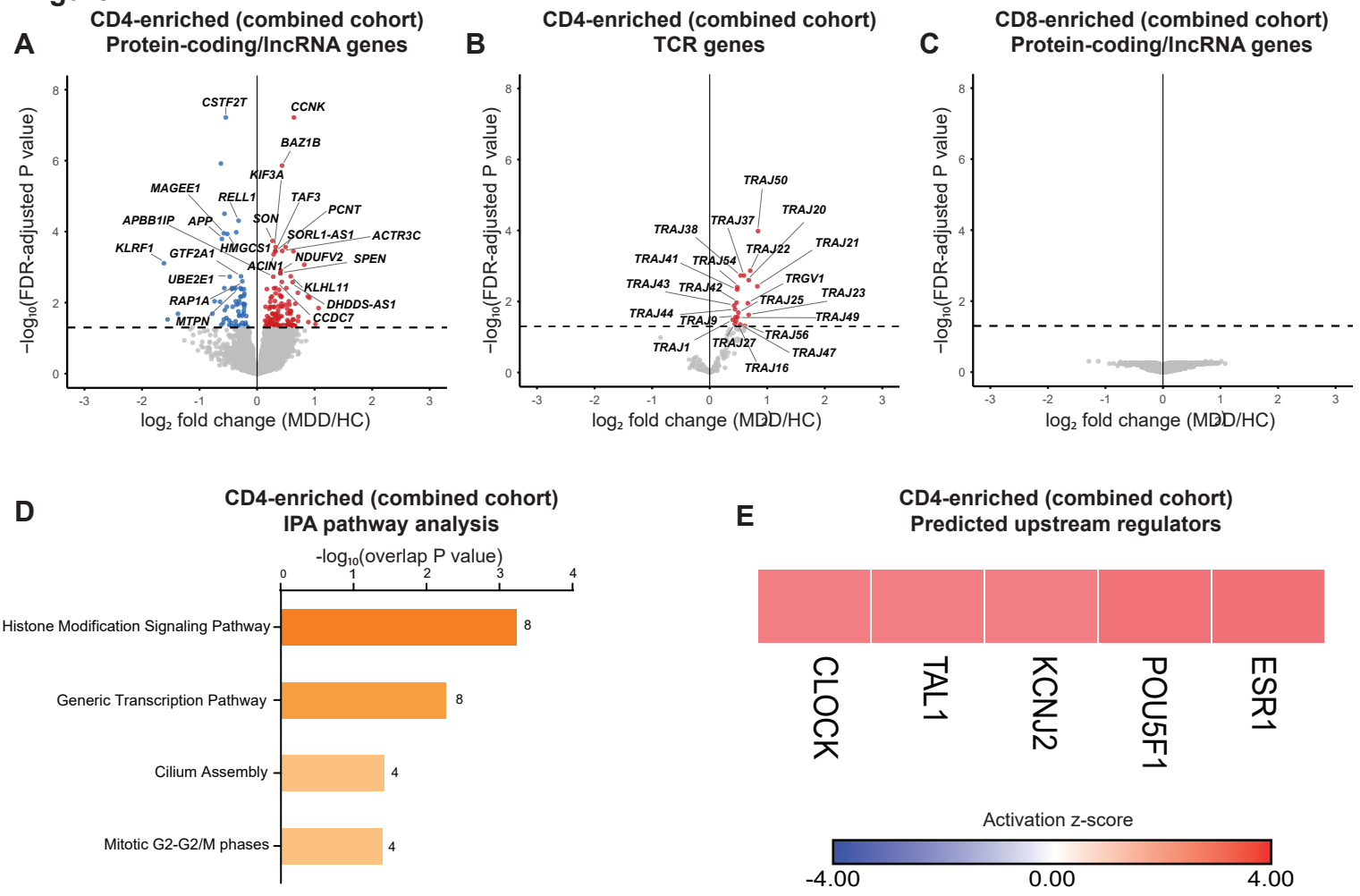

A
HC (48)
MDD (81)
PBMC isolation
Magnetic cell-sorting
RNA-seq
B
SSC-A
FSC-A
FSC-H
FSC-A
SSC-H
SSC-A
Viability-eFluor780
FSC-A
CD45-V500
CD3-BV421
CD8-BV785
CD4-APC
C
Total PBMCs
CD4-depleted cells
CD4-enriched cells
CD8-depleted cells
CD8-enriched cells
CD8-BV785
CD4-APC
D
CD4-enriched cells
CD8-enriched cells
CD4
CD8A
CD19
LILRA5
Log2(Read count + 1)
10
5
0

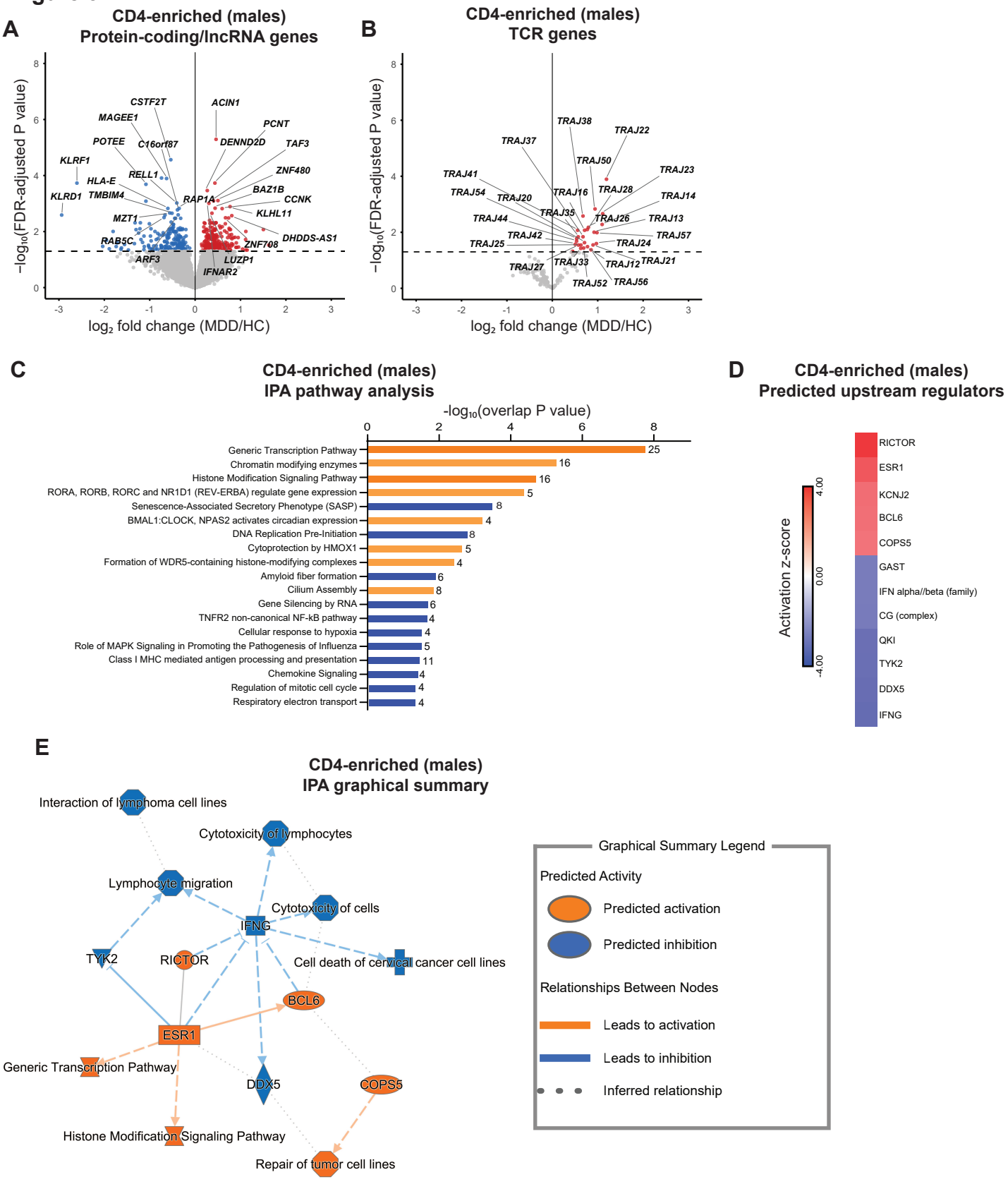
Figure 2


A
CD4-enriched (combined cohort)
Protein-coding/lncRNA genes
B
CD4-enriched (combined cohort)
TCR genes
C
CD8-enriched (combined cohort)
Protein-coding/lncRNA genes
−log10(FDR-adjusted P value)
log2 fold change (MDD/HC)
CSTF2T
CCNK
BAZ1B
KIF3A
MAGEE1
RELL1
TAF3
APBB1IP
APP
SON
PCNT
KLRF1
GTF2A1
HMGCS1
SORL1-AS1
ACTR3C
ACIN1
NDUFV2
SPEN
UBE2E1
KLHL11
RAP1A
DHDDS-AS1
MTPN
CCDC7
TRAJ50
TRAJ37
TRAJ20
TRAJ38
TRAJ22
TRAJ21
TRAJ41
TRAJ54
TRGV1
TRAJ43
TRAJ42
TRAJ25
TRAJ23
TRAJ44
TRAJ9
TRAJ49
TRAJ56
TRAJ1
TRAJ27
TRAJ47
TRAJ16

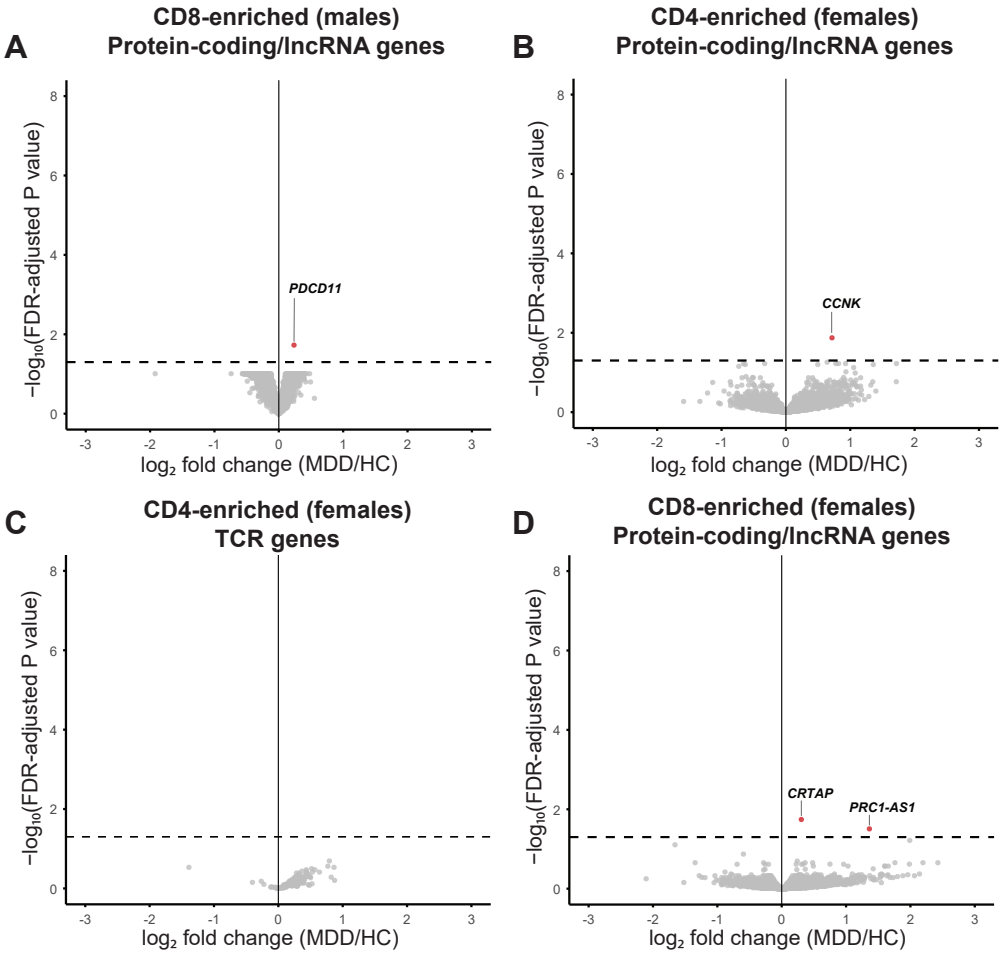
D
CD4-enriched (combined cohort)
IPA pathway analysis
-log10(overlap P value)
Histone Modification Signaling Pathway
Generic Transcription Pathway
Cilium Assembly
Mitotic G2-G2/M phases

E
CD4-enriched (combined cohort)
Predicted upstream regulators
CLOCK
TAL1
KCNJ2
POU5F1
ESR1
Activation z-score
-4.00
0.00
4.00

Figure 3


A
CD4-enriched (males)
Protein-coding/lncRNA genes
−log10(FDR-adjusted P value)
log2 fold change (MDD/HC)
CSTF2T
MAGEE1
POTEE
C16orf87
KLRF1
RELL1
HLA-E
KLRD1
TMBIM4
MZT1
RAB5C
ARF3
ACIN1
PCNT
DENND2D
TAF3
ZNF480
BAZ1B
RAP1A
CCNK
KLHL11
DHDDS-AS1
ZNF708
LUZP1
IFNAR2
B
CD4-enriched (males)
TCR genes
−log10(FDR-adjusted P value)
log2 fold change (MDD/HC)
TRAJ38
TRAJ22
TRAJ37
TRAJ50
TRAJ23
TRAJ41
TRAJ54
TRAJ20
TRAJ16
TRAJ28
TRAJ14
TRAJ35
TRAJ26
TRAJ13
TRAJ44
TRAJ42
TRAJ57
TRAJ25
TRAJ24
TRAJ27
TRAJ33
TRAJ12
TRAJ21
TRAJ52
TRAJ56
C
CD4-enriched (males)
IPA pathway analysis
-log10(overlap P value)
Generic Transcription Pathway 25
Chromatin modifying enzymes 16
Histone Modification Signaling Pathway 16
RORA, RORB, RORC and NR1D1 (REV-ERBA) regulate gene expression 5
Senescence-Associated Secretory Phenotype (SASP) 8
BMAL1:CLOCK, NPAS2 activates circadian expression 4
DNA Replication Pre-Initiation 8
Cytoprotection by HMOX1 5
Formation of WDR5-containing histone-modifying complexes 4
Amyloid fiber formation 6
Cilium Assembly 8
Gene Silencing by RNA 6
TNFR2 non-canonical NF-kB pathway 4
Cellular response to hypoxia 4
Role of MAPK Signaling in Promoting the Pathogenesis of Influenza 5
Class I MHC mediated antigen processing and presentation 11
Chemokine Signaling 4
Regulation of mitotic cell cycle 4
Respiratory electron transport 4
D
CD4-enriched (males)
Predicted upstream regulators
Activation z-score
4.00
0.00
-4.00
RICTOR
ESR1
KCNJ2
BCL6
COPS5
GAST
IFN alpha//beta (family)
CG (complex)
QKI
TYK2
DDX5
IFNG
E
CD4-enriched (males)
IPA graphical summary
Interaction of lymphoma cell lines
Cytotoxicity of lymphocytes
Lymphocyte migration
Cytotoxicity of cells
IFNG
TYK2
RICTOR
Cell death of cervical cancer cell lines
BCL6
ESR1
Generic Transcription Pathway
DDX5
COPS5
Histone Modification Signaling Pathway
Repair of tumor cell lines
Graphical Summary Legend
Predicted Activity
Predicted activation
Predicted inhibition
Relationships Between Nodes
Leads to activation
Leads to inhibition
Inferred relationship

Supplementary Figure 1



Supplementary Files

This is a list of supplementary files associated with this preprint. Click to download.

- Table.1.docx
- SupplementaryFiguresCaption.docx
- Figrue.S1GH.jpg
- Figure.S1EF.jpg
- Figure.S1CD.jpg
- Figure.S1AB.jpg
- ESMTableS1.PMAresults.xlsx
- ESMTableS2.FeZnSphaleriteGeothermometer.xlsx